

See discussions, stats, and author profiles for this publication at: <https://www.researchgate.net/publication/267984052>

Fully automatic segmentation of breast ultrasound images based on breast characteristics in space and frequency domains

Article in *Pattern Recognition* · February 2015

DOI: 10.1016/j.patcog.2014.07.026

CITATIONS

135

READS

3,289

3 authors:



Min Xian

University of Idaho

100 PUBLICATIONS 1,614 CITATIONS

[SEE PROFILE](#)



Yingtao Zhang

Harbin Institute of Technology

98 PUBLICATIONS 2,164 CITATIONS

[SEE PROFILE](#)



H.D. Cheng

Utah State University

303 PUBLICATIONS 14,679 CITATIONS

[SEE PROFILE](#)



Fully automatic segmentation of breast ultrasound images based on breast characteristics in space and frequency domains

Min Xian ^{a,b}, Yingtao Zhang ^b, H.D. Cheng ^{a,*}

^a Department of Computer Science, Utah State University, Logan, UT 84322, USA

^b School of Computer Science and Technology, Harbin Institute of Technology, Harbin 150001, China

ARTICLE INFO

Article history:

Received 18 February 2014

Received in revised form

25 May 2014

Accepted 12 July 2014

Available online 12 August 2014

Keywords:

Breast ultrasound (BUS) images

Computer-aided diagnosis (CAD)

Region of interest (ROI) generation

Automatic segmentation

ABSTRACT

Due to the complicated structure of breast and poor quality of ultrasound images, accurately and automatically locating regions of interest (ROIs) and segmenting tumors are challenging problems for breast ultrasound (BUS) computer-aided diagnosis systems. In this paper, we propose a fully automatic BUS image segmentation approach for performing accurate and robust ROI generation, and tumor segmentation. In the ROI generation step, the proposed adaptive reference point (RP) generation algorithm can produce the RPs automatically based on the breast anatomy; and the multipath search algorithm generates the seeds accurately and fast. In the tumor segmentation step, we propose a segmentation framework in which the cost function is defined in terms of tumor's boundary and region information in both frequency and space domains. First, the frequency constraint is built based on the newly proposed edge detector which is invariant to contrast and brightness; and then the tumor pose, position and intensity distribution are modeled to constrain the segmentation in the spatial domain. The well-designed cost function is graph-representable and its global optimum can be found. The proposed fully automatic segmentation method is applied to a BUS database with 184 cases (93 benign and 91 malignant), and the performance is evaluated by the area and boundary error metrics. Compared with the newly published fully automatic method, the proposed method is more accurate and robust in segmenting BUS images.

© 2014 Elsevier Ltd. All rights reserved.

1. Introduction

Occurring in high frequencies, breast cancer is one of the leading causes of cancer death among females worldwide [1,2]. Finding early signs and symptoms of breast cancer by clinical examination is the key to reduce the mortality [3,4], and breast ultrasound (BUS) is a major imaging modality for early detection [5]. However, clinical experience and expert knowledge are necessary to achieve correct diagnosis [1,6]. These make the human perception-based diagnosis suffer from considerable intra- and inter-observer variabilities. In order to overcome such drawback, computer-aided diagnosis (CAD) systems have been studied [7–10].

Segmentation is a critical step in a BUS CAD system. Manual segmentation methods are time-consuming and tedious, and suffer from great individual variability [11]. Semi-automatic segmentation methods solved the problem partially. Nevertheless, some interactions were still required which prevented the widespread applications of BUS CAD systems. Therefore, driven by clinical needs and related applications, it is necessary and essential to develop automatic

segmentation methods having the ability to reduce dependencies on operators and ultimately lead to a fully automated CAD system.

Automatic segmentation method usually refers to the segmentation process requiring little user intervention or no intervention at all; the former is called semi-automatic segmentation, while the latter is called fully automatic segmentation. The fully automatic methods are characterized by the prior constraints, such as shape, appearance and spatial location of the lesions. Several works discussed fully automatic segmentation for BUS images [13–17].

In [14], it employed gray-level gradient as segmentation constraint to detect tumors on BUS images automatically. The method located ROIs by the radial gradient index (RGI) filtering technique. The points of interest (POIs) at the centers of the ROIs were selected as the seeds; then a region growing algorithm based on the maximum average radial gradient (ARD) was applied to obtain the tumor contours. The method was tested on a database of 400 patients (757 images) and 75% tumors were correctly detected at an overlap of 0.4 with radiologist tumor outlines.

In [15], the authors proposed a hybrid completely automatic segmentation method which combined the region-based and boundary-based techniques. They developed a mathematical formulation of the empirical rules (intensity, texture and location) to generate tumor seeds automatically. Region growing and

* Corresponding author. Tel.: +1 435 7972054; fax: +1 435 7973265.

E-mail address: hengda.cheng@usu.edu (H.D. Cheng).

directional gradient of the image were used to find the boundary points after seed generation. Then, a rule based on Euclidean distances between candidate boundary points and the seed were employed to refine the boundary points by eliminating the outliers. Finally, the refined boundary points serve as the initial boundary of a deformable model. Area error metrics were used to measure the performance of the algorithm on 42 BUS images, the true positive ratio (TPR) was 75.04%, false positive ratio (FPR) was 20.86%, and false negative ratio (FNR) was 24.96%, respectively.

Liu et al. [16] described a fully automatic method based on an active contour mode. The method was divided into two steps: ROI generation and ROI segmentation steps. In the first step, a supervised local texture classifier (a support vector machine) was trained to find the candidate ROIs. Vertical position and distance to the image center were employed to determine the final ROI. In the second step, it used an active contour model which combined the global statistical information and local edge information to locate the final tumor contour. The performance was evaluated by using area error metrics on a database of 103 BUS images (48 benign and 55 malignant) and the TPR was 91.31%, FPR was 8.69% and FNR was 7.26%, respectively.

Shan et al. [12] proposed an automatic seed point selection algorithm. The method formulated the texture, spatial location and size of the candidate area. It ranked the regions obtained from the iterative thresholding by the empirical formula, and selected the center of the winning region as the seed. Then, a fully automatic segmentation method was developed based on the features from the spatial and frequency domains [13,17]. Two new features called phase in max-energy orientation (PMO) and radial distance (RD) were proposed. Combing with common texture and gray level features [15], the new feature set was utilized to classify tumor pixels from the background by a trained ANN. The algorithm was tested on a database of 60 BUS images. It achieved a TPR of 93.41%, FPR of 12.72% and FNR of 6.59% by using the area error metrics; and an average Hausdorff error (AHE) of 18.90 pixels and an average mean absolute error (AME) of 5.04 pixels by using the boundary error metrics.

Notice that the methods mentioned above are all followed a two-step strategy: first, locating the ROI, and then segmenting the tumor in the ROI. Although some of the fully automatic methods have achieved quite good performance on their own datasets, these methods still suffer from some drawbacks, which impede the widespread application of BUS CAD systems.

- 1) **Lack of biological foundations.** Some existing BUS segmentation methods [14,18–22] applied computer vision, image processing, pattern recognition and machine learning algorithms for processing BUS images. However, without incorporating with the biological background of the breast, the BUS CAD systems cannot work well.
- 2) **Non-robust constraints.** Although some fully automatic segmentation methods employed biological knowledge of breast explicitly or implicitly, most of the ROI generation methods [13–17] were dependent on certain hard or inflexible constraints, such as the fixed reference points (RPs) for selecting seeds or ROIs [14], fixed gray value for thresholding, fixed region size and spatial location for refining candidate ROIs [16], which make these methods difficult to achieve good generalization ability. For example, a fixed RP in the middle of the image may result wrong tumor detection, if the tumor is far away from the center of the image.
- 3) **Low ability to exclude structures similar to tumors.** The methods [10,16] relying only on the tumor features from the spatial domain cannot effectively distinguish the tumors from the hypoechoic neighboring regions, such as fat regions and shadowing artifacts.

To solve above problems, an accurate, robust, and fast fully automatic segmentation method is proposed in this paper. In the ROI generation step, the newly proposed adaptive RP generation algorithm and the multipath search algorithm can locate the tumor region quickly without utilizing any fixed and inflexible constraints. In the second step, we proposed a segmentation framework, which utilized the edge information in the frequency domain and information of the intensity distribution, position and pose of tumors in the space domain. It has high ability to exclude normal region from tumor region. The flowchart of the proposed approach is illustrated in Fig. 1.

The paper is organized as follows: in Section 2, the fully automatic ROI generation algorithm is presented; in Section 3, the segmentation method is illustrated; in Section 4, the experimental results are discussed; and the conclusion is given in Section 5.

2. Fully automatic ROI generation

ROI generation is a prerequisite step for automatic segmentation and classification in many BUS CAD systems. A ROI is usually a rectangular region [10,13,16,17] which provides the rough location of a lesion and excludes normal tissues as much as possible. In [10,16], a supervised local texture classifier was proposed to find the candidate ROIs, and the fixed constraints, such as region size and spatial location, were used to select the final ROI. In [14], the authors located ROIs by using RGI filtering method and gray level thresholding, and the constraining function and the threshold must be predefined. In [13,17], the authors proposed an iterative threshold selecting method to locate the ROIs, and the final ROI was selected based on the region size and the distance between the candidate region and the fixed reference point (image center). We can see that the inflexible constraints used in the above automatic ROI generation methods reduced their robustness. An ideal automatic ROI generation method should have the following characteristics:

- 1) **Fully automatic.** The operator-independent feature can avoid the subjective bias and tedious work caused by manual and semi-automatic methods.
- 2) **Complete coverage of tumor region.** It is the necessary condition for achieving high segmentation accuracy.

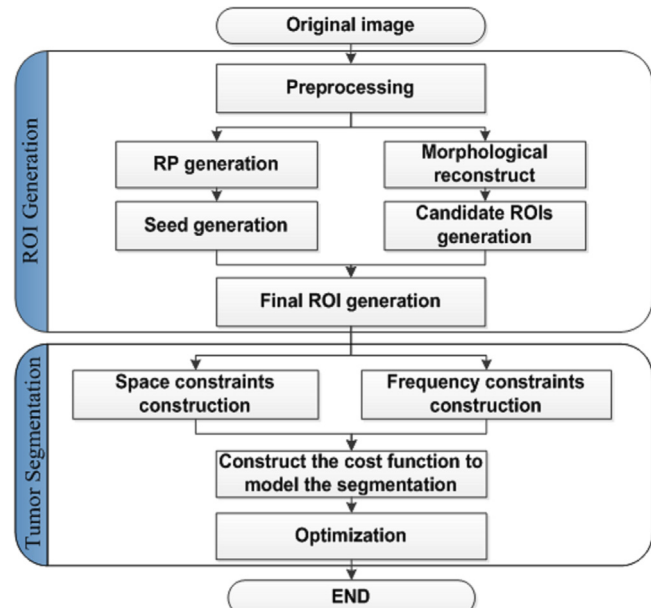


Fig. 1. Flowchart of the proposed segmentation method.

- 3) **High discriminating ability.** Some normal regions (subcutaneous and retromammary fat regions) on BUS images can cause the failure of many segmentation methods. An ideal ROI generation method should be able to exclude such regions as much as possible.
- 4) **Flexible constraints for segmentation.** The constraints based on empirical domain knowledge must be flexible to make the methods robust and adaptive, and achieve high generalization ability.

Now, we propose a fully automatic and adaptive ROI generation method which needs no operator intervention during the entire process and can produce RPs automatically without any hard constraints. The proposed multipath search algorithm can generate the seed accurately, and can distinguish the tumor regions from normal regions accurately.

2.1. Preprocessing

The breast tumor reflects lower level of echoes than surrounding tissues, and appears relatively darker (hypoechoic) on BUS image [6]. However, the gray levels, contrast, texture, etc. of B-mode BUS images vary greatly due to the facts that they are operator-dependent and device-dependent. The preprocessing is to normalize intensities and to enhance the hypoechoic regions

(candidates of tumor regions). The proposed preprocessing steps are as below:

- 1) **Smoothing.** A 2-D discrete Gaussian low-pass filter was utilized to smooth the BUS image in the frequency domain (using fast Fourier transform) [24]. Fig. 2(a) shows an example of Gaussian low-pass filter with size 300×300 and its cutoff frequency is 30.
- 2) **Eliminating the intensity range variability.** Similar to [10], we applied a linear normalization to align the lower and upper bounds. The linear normalization is defined as below:

$$f_{L_{norm}} = \begin{cases} 0, & \text{if } x \leq l_{bound} \\ \frac{(x - l_{bound})(L_n - 1)}{u_{bound} - l_{bound}}, & \text{if } l_{bound} \leq x \leq u_{bound} \\ L_n - 1, & \text{if } x \geq u_{bound} \end{cases} \quad (1)$$

In Eq. (1), L_n is the number of gray levels; l_{bound} and u_{bound} are defined as $Q(0.5)$ and $Q(0.95)$, respectively. Q is the quantile function on the cumulative distribution of the histogram.

$$Z(x; z_a, z_b, z_c) = \begin{cases} 1, & \text{if } x \leq z_a \\ 1 - \frac{(x - z_a)^2}{(z_c - z_a)(z_b - z_a)}, & \text{if } z_a \leq x \leq z_b \\ \frac{(x - z_c)^2}{(z_c - z_a)(z_c - z_b)}, & \text{if } z_b \leq x \leq z_c \\ 0, & \text{if otherwise} \end{cases} \quad (2)$$

- 3) **Enhancing hypoechoic regions.** An adaptive Z-shaped function (Eq. (2)) was proposed to reverse the intensities and

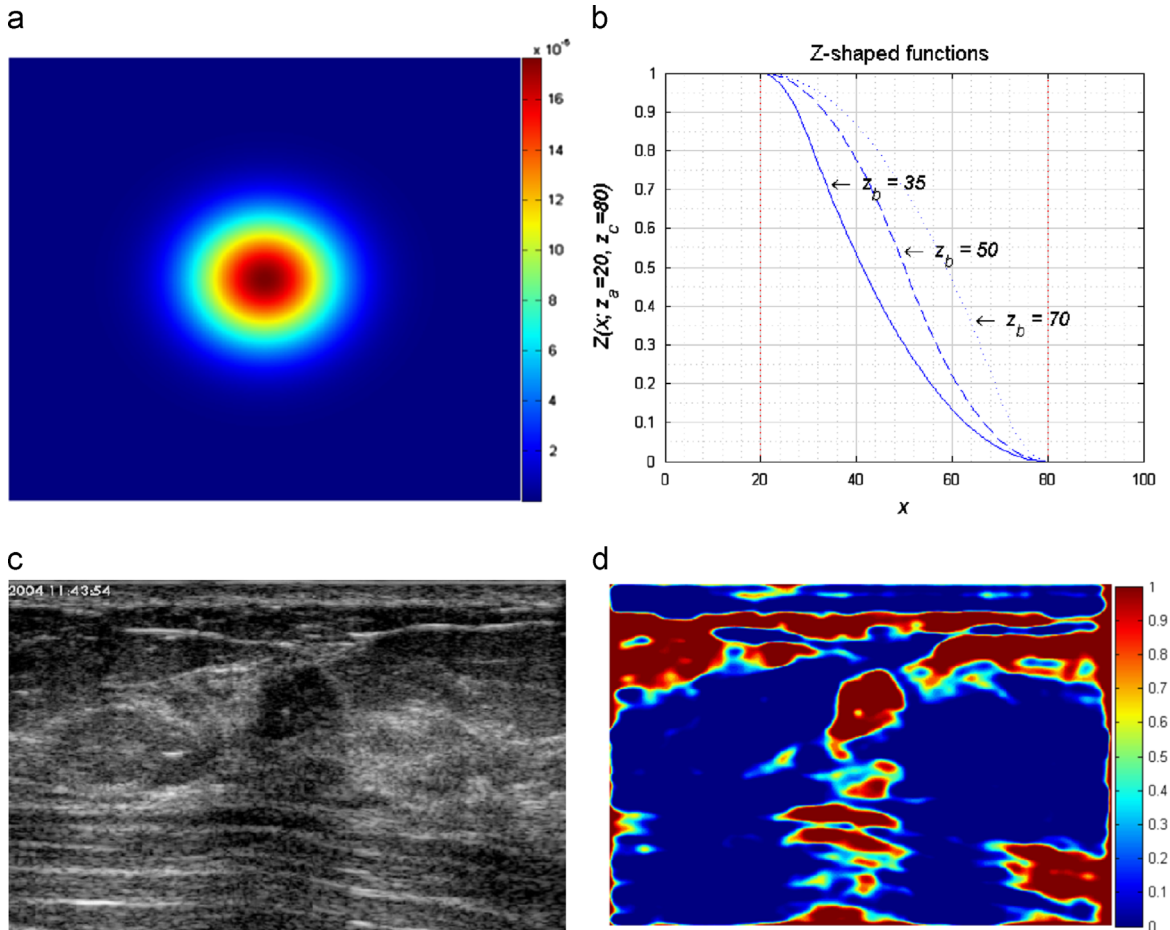


Fig. 2. (a) A discrete Gaussian low-pass filter with $M=N=300$, $d_0=30$; (b) three Z-shaped functions with $z_a=20$, $z_b=\{35, 50, 70\}$ and $z_c=80$; (c) a BUS image; (d) the result of the preprocessing.

transform them into [0, 1]. The shape of the function is determined by the characteristics of image adaptively. Fig. 2(b) plots three Z-shaped functions with $z_a=20$ and $z_c=80$, and three different z_b values. In Eq. (2), the parameters, z_a and z_c , determine the nonlinear range of the curve; the parameter z_b is used to adjust the steepness of the curve which should be decided adaptively according to the skewness of the intensity distribution:

$$z_b = \begin{cases} (z_a+z_c)/2, & \text{if } SN \leq 0 \\ [z_a+z_c(1-SN)]/2, & \text{if } SN > 0 \end{cases} \quad (3)$$

$$SN = \frac{\sqrt{(n-1)(n-2)}}{n} \frac{1/n \sum_{i=1}^n (x_i - \bar{x})^3}{\left[1/n \sum_{i=1}^n (x_i - \bar{x})^2 \right]^{3/2}} \quad (4)$$

where x_i is the intensity of the i th pixel, \bar{x} is mean of image intensities, n is the number of pixels, z_c is determined by the mean of the intensities, and z_a is a constant set as 20. SN is the bias-corrected skewness [25] which measures the asymmetry of the image intensity distribution. The larger the skewness (SN) becomes, the more the mass of the distribution concentrates on the left side, which will result a steeper Z-shaped function (small z_b). As shown in Fig. 2(d), a steep Z-shaped function can enhance hypoechoic regions of Fig. 2(c) significantly by compressing the higher-level intensities.

In order to make the details more visible, Figs. 2(a,d) and 3(b-f) are shown in pseudo-colors, and the corresponding scales are shown by the color bars.

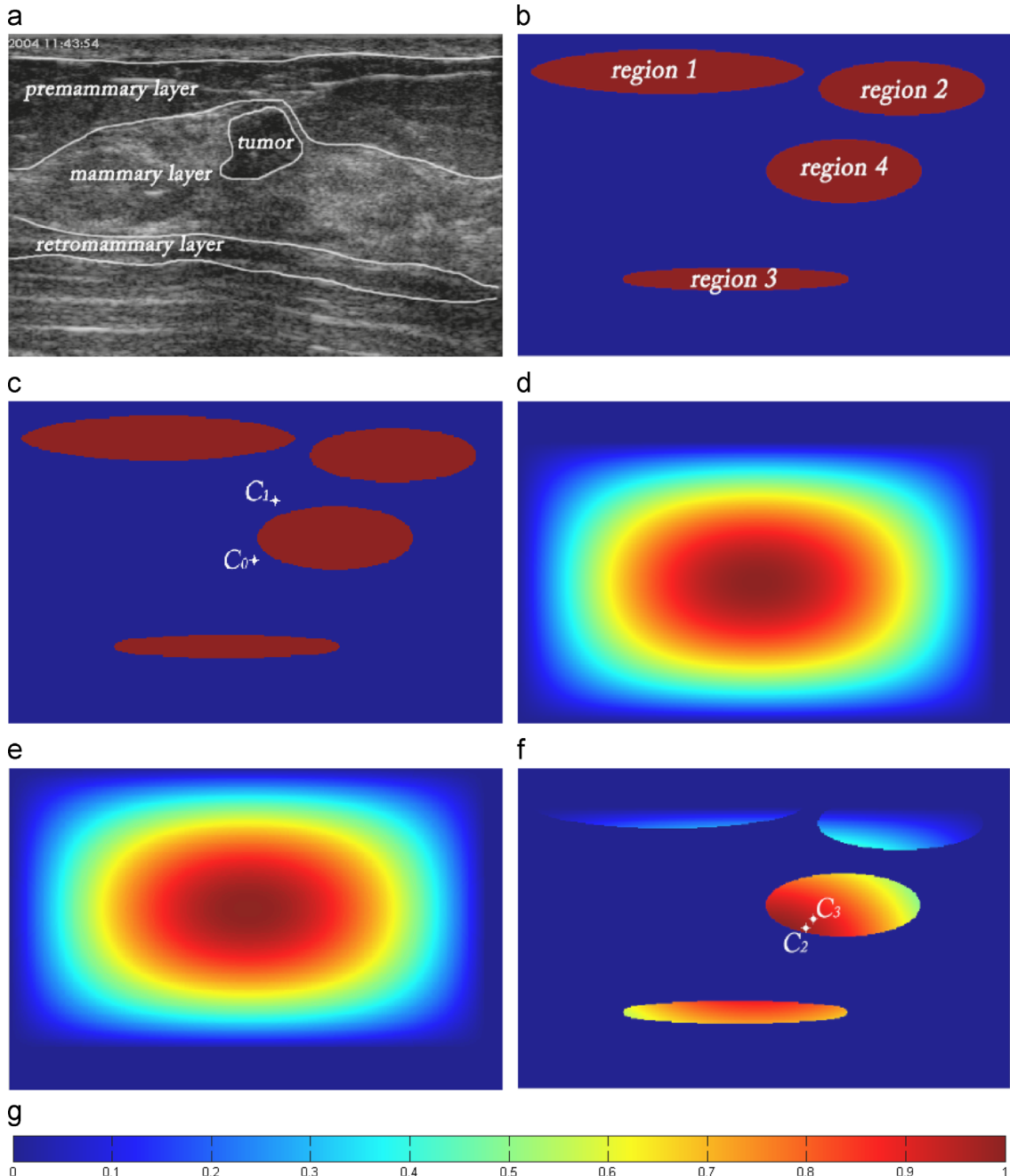


Fig. 3. (a) Three major layers of the breast in a BUS image; (b) a synthetic image ($M=300, N=500$); (c) C_0 and C_1 ; (d) w_1 with $X_1^L=1, X_1^R=14, Y_1^T=38$, and $Y_1^D=1$; (e) w_2 with $X_1^L=1, X_1^R=16, Y_1^T=1$, and $Y_1^D=38$; (f) C_2 and C_3 on the image generated by the third iteration of Algorithm 1; (g) the color bar.

2.2. Adaptive reference point generation based on breast anatomy

A reference point (RP) is a position in a BUS image for ranking other pixels or regions. If a pixel is close to the RP, it will have a large probability to be in the lesion. In many fully automatic segmentation methods [12,14,15,17], the RP was defined as a pixel at the fixed position, which led the failure of these algorithms when the actual tumor location was far away from the predefined RP. In this section, we propose a novel algorithm (**Algorithm 1**) for selecting RP from the preprocessed image automatically and adaptively. The biological foundation for the proposed method is based on [26]: the breast has three major layers from the skin of the breast: the premammary (PM) layer, the mammary layer, and the retromammary (RM) layer (Fig. 3(a)); the PM layer lies between the skin and the mammary layer, and contains subcutaneous fat mainly; the mammary layer is in the middle of the three layers, and breast tumors arise in this layer; and the RM layer lies between the mammary layer and the chest wall and contains mainly the fat as well.

Now we propose two definitions for **Algorithm 1**. The first definition is the weighted *density center* which will move to the tumor regions iteratively. The origin of the image coordinates is at the top-left corner. The weighted density center at the *i*th iteration is defined as

$$C_i = \frac{\sum_{x,y} \left(\prod_{j=0}^{i-1} w_j(x,y) \right) I'(x,y)}{\sum_{x,y} \left(\prod_{j=0}^{i-1} w_j(x,y) \right)}, \quad x = 1, 2, \dots, M, \text{ and} \\ y = 1, 2, \dots, N \quad (5)$$

where (x, y) are the coordinates of the pixel, I' is the image after preprocessing, w_j is the *j*th weighting function, and M and N are the numbers of rows and columns of the image, respectively. The initial center C_0 is defined as the geometric center of the image and the number of weighted density centers will be determined by **Algorithm 1**.

In Eq. (5), without considering the influence of the weighting functions, center C_i will move to the higher intensity region of I' . However, the fats in the PM and RM layers also have high intensities in the preprocessed image (Fig. 2(d)), which make C_i diverge from the real tumor region. The weighting function is proposed to solve the above problem based on the fact that these normal regions are mainly from the fats in PM and RM layers, while the mammary layer lies in their middle. The weighting function is proposed to attenuate the intensities of the surrounding regions and the *i*th weighting function is defined as

$$w_i(x,y) = \begin{cases} 0, & \left(\begin{array}{l} x < X_i^L \text{ or } x > N - X_i^R \text{ or} \\ y < Y_i^T \text{ or } y > M - Y_i^D \end{array} \right) \\ \frac{(x - X_i^L) \cdot (N - X_i^R - x)}{[(N - X_i^L - X_i^R)/2]^2} \cdot \frac{(y - Y_i^T) \cdot (M - Y_i^D - y)}{[(M - Y_i^T - Y_i^D)/2]^2}, & \text{otherwise} \end{cases} \quad (6)$$

where X_i^L, X_i^R, Y_i^T and Y_i^D are the distances between the bounds of the *i*th weighting function and their corresponding borders (left: 1, right: M , top: 1, and bottom: N) of the image, respectively. The values of X_i^L, X_i^R, Y_i^T and Y_i^D are updated according to the weighted density centers iteratively. The initial weight w_0 is a matrix with all elements equal to 1.

Algorithm 1. RP generation

Inputs: C_0, w_0, I'

Output: the position of RP: RP_0

1. For $i=1$: N_{MAX}
2. Calculate new center C_i using Eq. (5), and $RP_0 \leftarrow C_i$;
3. If $\|C_i - C_{i-1}\| < \epsilon_1$ then

4. break;
5. Else
6. Update the bounds $(X_i^L, X_i^R, Y_i^T, \text{ and } Y_i^D)$ of the weighting function:
7. If $C_i^X - C_{i-1}^X > 0$ then $X_i^L = C_i^X - C_{i-1}^X, X_i^R = X_{i-1}^R$
8. Else $X_i^L = X_{i-1}^L, X_i^R = C_{i-1}^X - C_i^X$
9. If $C_i^Y - C_{i-1}^Y > 0$ then $Y_i^T = C_i^Y - C_{i-1}^Y, Y_i^D = Y_{i-1}^D$
10. Else $Y_i^T = Y_{i-1}^T, Y_i^D = C_{i-1}^Y - C_i^Y$
11. Update the weighting function w_i using Eq. (6);
12. End
13. Return RP_0 .

In **Algorithm 1**, the RP is generated by updating the weighting functions and weighted density centers iteratively. The algorithm will stop when it reaches the maximum number of iterations (N_{MAX}) or the Euclidean distance between two adjacent weighted density centers is smaller than a predefined value ϵ_1 ($N_{MAX}=100$ and $\epsilon_1=2$ in all of the experiments). (C_i^X, C_i^Y) and (C_{i-1}^X, C_{i-1}^Y) represent the coordinates of the weighted density centers at the *i*th and the $(i-1)$ th iterations, respectively. In order to explain the procedure of **Algorithm 1** clearly, we applied the algorithm to generate RP of a synthetic image (Fig. 3); and the RP generation results of real B-mode BUS images are shown in Fig. 4.

As shown in Fig. 2(d), the intensities of the fat regions in the PM and RM layers are similar to those of the tumor. In Fig. 3(b), regions 1–3 are used to simulate the fat regions around the mammary layer (middle layer); region 4 is the tumor in the mammary layer. Because the four regions are distributed mainly in the top right part of the image, the weighted density center C_1 moves to the upper right of C_0 (Fig. 3(c)). As shown in Fig. 3(d and e), the weighting function w_1 and w_2 are applied to correct the deviation by moving the center of the weighting functions to the lower left and the upper left, respectively. Fig. 3(f) shows that the intensities of the three regions (regions 1–3) around the target (region 4) are attenuated after the third iteration, and C_2 and C_3 are already in the target region.

2.3. Seed generation

In this section, we will use the RP as the initial point to search the seed. We develop a multipath search algorithm to obtain the seed in the tumor. The advantages of the proposed algorithm are (1) the seed is generated iteratively based on the local mean of intensities rather than heavily depended on the distances between the RP and the candidate regions [12,15], which will be more accurate than the existing methods (refer Fig. 4), and (2) it generates the seed with high speed (refer Table 1).

In **Algorithm 2**, RP_0 is the final reference point and I' is the preprocessed image. We extend the reference point into multiple points along the *i*th direction:

$$RP_i = RP_0 + h(\cos \theta_i, \sin \theta_i), \quad i = 1, 2, \dots, n_{dre} \quad (7)$$

$$\theta_i = 2\pi(i-1)/n_{dre} \quad (8)$$

where n_{dre} is the number of directions, θ_i denotes the angle of the *i*th direction relative to RP_0 , and h is the step size (12 pixels) determined by experiments.

Algorithm 2. Seed generation

Inputs: RP_0, I'

Output: seed

1. Extend RP_0 to N_{rp} RPs
2. Initialize an array c with size N_{rp} to save the candidate positions;
3. For $i=1$: N_{rp}
4. Initialize the start position p to be RP_i ;

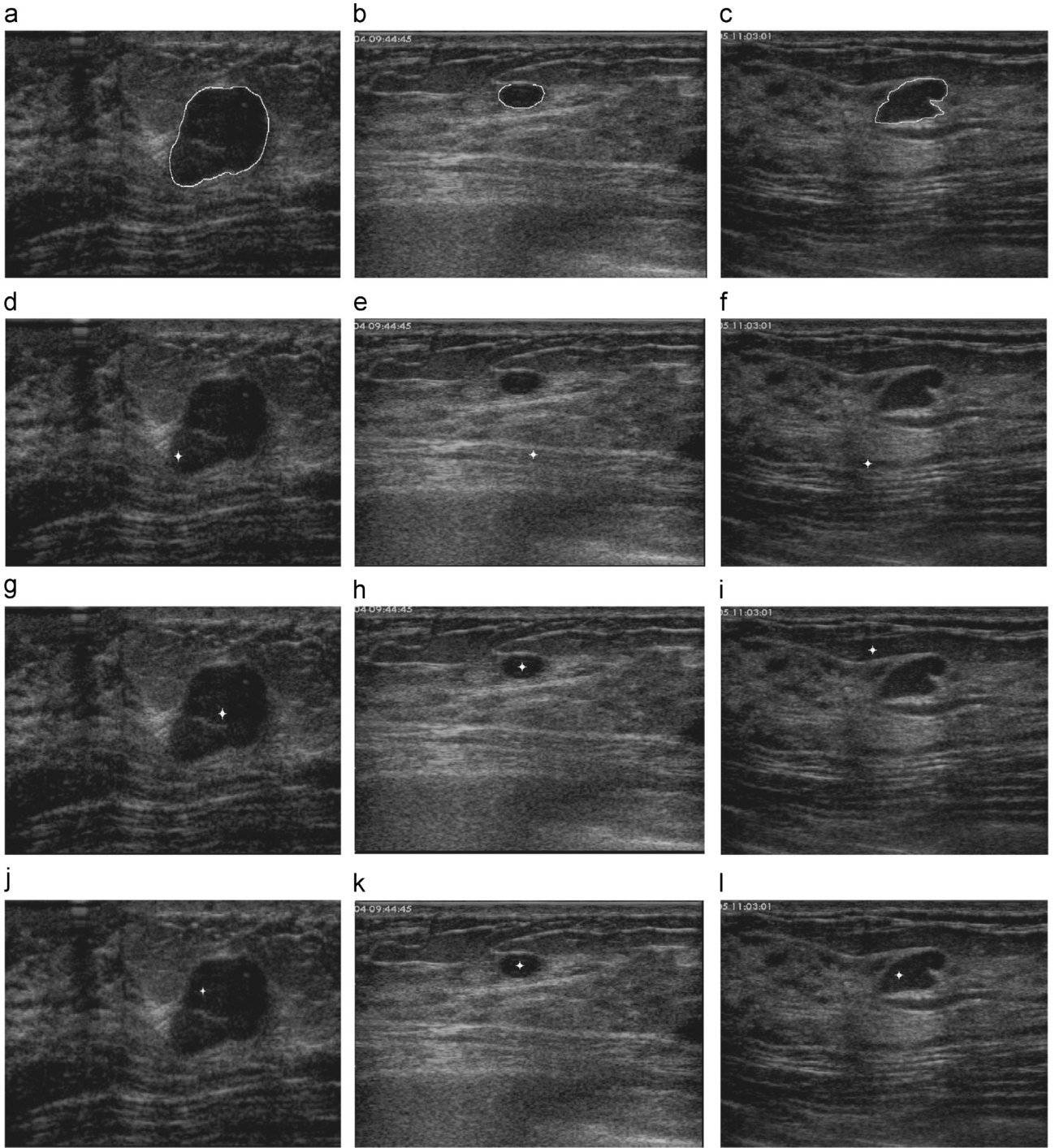


Fig. 4. The seed generation of four BUS images: (a)–(c) the original images with delineations by an experienced radiologist; (d)–(f) the seeds generated by the method in [15]; (g)–(i) the seeds generated by the method in [17]. (j)–(l) the seeds generated by the proposed method.

5. Iterate until converge to a candidate position $c[i]$:
6. Calculate next position $next(p)$ using Eq. (9);
7. If $\|next(p) - p\| < \varepsilon_2$ then $c[i] \leftarrow p$; break current iteration;
8. Else $p \leftarrow next(p)$;
9. End
10. Choose the point in c with the maximum local mean (using Eq. (12)) as the final seed.

and $next(p)$ is defined as [28]

$$next(p) = \frac{\sum_{i=1}^n K_H(p_i - p) l'(p_i)p_i}{\sum_{i=1}^n K_H(p_i - p) l'(p_i)} \quad (9)$$

where l' is the normalized image, p_i is the coordinate of the i th point of l' , and K_H is a kernel function defined as

$$K_H(p_i - p) = F[H^{(-1/2)} \times (p_i - p)] \quad (10)$$

In Eq. (10), H is a bandwidth matrix, $H = diag(h^2, h^2)$ and F is the unit flat kernel [27] centered at position p . After the iterations on each RP , we obtain N_{rp} candidate seeds. The one with the

Mean shift [27,28] is utilized to calculate the next position of the current point (Eq. (9)). We shift position p to a new position $next(p)$ when their distance is larger than a predefined value (ε_2),

maximum local sum of intensities will be the final seed

$$\text{seed} = \underset{p}{\operatorname{argmax}}(M(p)), p \in \{c[i] | i = 1, 2, \dots, N_{\text{tp}}\} \quad (11)$$

$$M(p) = \sum_{i=1}^n K_H(p_i - p) I'(p_i) \quad (12)$$

where $M(p)$ is the local mean of the candidate seeds. The predefined value $\varepsilon_2 = 2$ determined by experiments.

2.4. Candidate ROIs generation

Because of the inhomogeneity of the tumor region, peaks and dark regions may exist in the tumor area, which will make it difficult to extract the whole tumor region from its background by thresholding only. The morphological reconstruction [29] based on opening and closing was employed to spread out the peaks and remove the small dark or bright points. The reconstruction operators are defined as

$$I_{ro} = R(I' \circledast se), I_{rc} = R((I_{ro})^c, (I_{ro} \oplus se)^c), I_{final} = (I_{rc})^c \quad (13)$$

where se is the disk shaped structuring element whose radius is 16 (pixels), $R(X, Y)$ denotes the reconstruction of the “mask” image X from “maker” image Y . The symbols \circledast, \oplus , and c denote the erosion, dilation, and complement operators, respectively.

The Otsu automatic thresholding operation [30] is performed on the I_{final} to extract the suspicious tumor regions SR .

2.5. ROI selection

Based on the set of candidate regions SR , the original ROI (ROI_0) will be chosen by using Eq. (14).

$$ROI_0 = \{x \in R | (R \in SR) \wedge (\text{seed} \neq \emptyset) \wedge (\text{seed} \in R)\} \quad (14)$$

$$ROI_t = \left\{ \begin{array}{l} p = (p_x, p_y) | p_x \geq \max(x_{tl} - d, 1) \wedge \\ p_y \geq \max(y_{tl} - d, 1) \wedge \\ p_x \leq \min(x_{tl} + ht + d, M) \wedge \\ p_y \leq \min(y_{tl} + wd + d, N) \end{array} \right\} \quad (15)$$

In Eq. (14), R represents any candidate region in set SR . Let x_{tl} and y_{tl} be the minimal vertical and horizontal coordinates of region ROI_0 ; and ht and wd be the height and width of the bounding box of ROI_0 . The final ROI (ROI_t) is a rectangle and defined by Eq. (15) where d is a constant selected as 50 (pixels) which is large enough to cover the tumors completely.

3. Tumor segmentation based on the newly proposed segmentation framework

Image segmentation is an ill-posed problem. In order to solve this kind of problems, regularization process is needed to involve specific task-related knowledge [31]; for instance, in BUS image segmentation, the gray level distribution, intensity gradient, texture, local image phase, and tumor shape are commonly used [32].

In order to take advantage of the features in both the spatial and frequency domains, several works have studied on integrated spatial and frequency domain features for segmentation. In [13,17], the authors combined the phase information in the frequency domain with the radial distance and texture features in the spatial domain, and classified breast tumor pixels from the background by a trained ANN. In [38,39], the Fourier translation between two adjacent frames was calculated to estimate the object motion, and then the spatial information is used to segment the object. In [40], the authors extracted the texture features by combining the responses of Gabor filters in the frequency with the color in the

spatial domain, and segmented the color texture images in a MRF model.

In this section, we present a robust tumor segmentation approach built under the newly proposed segmentation framework. The main contributions of the proposed approach are (1) proposing a segmentation framework capable of handling boundary and region information in both the frequency and space domains, (2) proposing a novel edge detector in the frequency domain, and (3) building the space constraints (tumor position, pose and intensity distribution) in a flexible manner.

3.1. Proposed segmentation framework

This section discusses a segmentation framework which defines a cost function based on the constraints from both the space domain and frequency domain; and the cost function is modeled in terms of objects' region and boundary features. The proposed image segmentation framework includes five main components:

- 1) Set $S = \{s_1, s_2, \dots, s_M\}$ containing all pixels in the final ROI.
- 2) A neighborhood system $N = \{N_s | s \in S\}$, N_s defines the neighbors of pixel s .
- 3) A label set $L = \{l_1, l_2, \dots, l_c\}$.
- 4) A set $f = \{f_s | f_s \in L, s \in S\}$ specifies labels to pixels in image, and
- 5) A cost function E utilizes the space and frequency domain information, E^{SC} and E^{FC} , respectively. The optimal segmentation is obtained by minimizing the cost function E .

In the neighborhood system, N_s is defined as a set comprising eight pixels surrounding s . In the breast tumor segmentation task, the label set $L = \{l_1 = \mathbf{1}, l_2 = \mathbf{0}\}$. Labels $\mathbf{1}$ and $\mathbf{0}$ are for pixels in tumor and normal regions, respectively. The set f is defined as a mapping from S to L ; the cost function $E(f|y_{ROI})$, as shown in Eq. (16), is represented by a combination of two constraints from the space and frequency domains. Here, y_{ROI} represents the pixels in ROI_t of image y and is automatically located by the method described in Section 2.

$$E(f|y_{ROI}) = \lambda \cdot E^{SC}(f|y_{ROI}) + E^{FC}(f|y_{ROI}), \lambda \geq 0 \quad (16)$$

The term E^{FC} (defined in Section 3.2) is based on the newly proposed edge detector in the frequency domain, which is independent of image contrast and brightness: E^{FC} is large when the boundary defined by f crosses smooth regions, which will constrain the final boundary along the edges in the frequency domain.

The term E^{SC} (defined in Section 3.3) models the intensity distribution, position, and pose of the object in the space domain. It models the region and boundary properties by the first order and second order terms. The first order term defines how the intensity, pose and position of a pixel fit into a model; and the second order term penalizes the disconnectedness between neighboring pixels. The relative importance between the space domain and frequency domain is specified by the tuning parameter λ which will be discussed in Section 4.4.1.

3.2. Frequency constraint based on a novel edge detector

Many BUS imaging systems need operators to adjust the contrast by setting gain values manually. Therefore, BUS images may have different brightness and contrast. Meanwhile, the classical, space domain-oriented, and gradient-based segmentation algorithms may be affected by the changes in intensity and contrast. Therefore, we should have more robust methods.

In this section, we propose a novel edge detector to establish the edge constraint in the frequency domain which is invariant to contrast and brightness.

3.2.1. A novel edge detector for frequency constraint

The phase congruency [33–35] and zero-crossing [36] have been widely applied in image processing because they are invariant to image contrast and brightness; and high phase congruency and zero-crossing are important indicators of edges. We proposed a novel edge detector to find the step edges in BUS images. The edge detector is designed to assess the possibility of an edge between two adjacent points. The frequency constrain E^{FC} forces the final tumor boundary along the edges detected by the newly proposed edge detector.

In order to calculate the phase congruency, Kovesi [35] proposed a method by convolving a bank of log-Gabor filters with the image. The scale and orientation with the maximum log-Gabor filter responses reveal the smoothness and the orientation of the edge in a local area. For example, if a point on an edge has large response of a filter with large scale, the edge segment around the point must be smooth. On the other hand, if the point has large response of a filter with small scale, the edge is unsmooth; if the point has large response of a filter with orientation angle θ , and the direction of the local edge segment is close to θ . If the scale and the orientation of the tumor edge match those of a filter, the local response of the filter will be the maximum. Therefore, as shown in Eq. (17), we choose the scale (ns) and orientation (no) of a log-Gabor filter with the maximum real part energy ($e_{ns,no}$) to represent the edge scale and orientation at a point.

$$(s_i, n_i) = \arg \max_{ns, no} \{e_{ns,no}(i)\}, i \in S \quad (17)$$

The newly proposed edge detector ED will integrate the phase congruency information and zero-crossing on the scale and orientation with the maximum log-Gabor responses, and ED is defined as

$$ED(i, j) = ZC(i, j) \max(PCM(i), PCM(j)), j \in N_i, i \in S \quad (18)$$

In Eq. (18), $ED(i, j) \in [0, 1]$ evaluates the possibility of an edge between points i and j by using the zero crossing detector (ZC) and the phase congruency with the maximum energy response (PCM) over all scales and orientations.

ZC is defined as

$$ZC(i, j) = \frac{1}{2}[1 - sign(e_{(s_i, n_i)}(i)) \cdot sign(e_{(s_j, n_j)}(j))], j \in N_i, i \in S \quad (19)$$

In Eq. (19), ZC decides whether there exists an edge between points i and j . If the signs of $e_{(s_i, n_i)}$ and $e_{(s_j, n_j)}$ are the same, $ZC(i, j)$ is 0; if the signs are different, $ZC(i, j)$ is 1.

The PCM is defined as [23]

$$PCM(i) = |\cos[\phi_{(s_i, n_i)}(i)]|PC(i), i \in S \quad (20)$$

In Eq. (20), $PCM(i)$ detects the step edges with phase 0 and π , and is constructed in a soft manner, which is capable of detecting blur edges (phase close to 0 or π). $\phi_{(s_i, n_i)}$ denotes the phase of the i th point. $PC(i)$ is the phase congruency of point i [35].

The cost function term E^{FC} in Eq. (21) models the frequency constraints. It penalizes the inconsistency between the final boundary and the edges detected by ED . If the boundary of the segmented tumor cross a smooth region and ED will be small, then the segmentation has high penalty; while the segmentation cross the regions with high ED value, it has small penalty. Therefore, the frequency constraint E^{FC} will force the segments to follow the edges with high ED values.

$$E^{FC}(f|y_{ROI}) = \sum_{i \in S} \sum_{j \in N_i} V_{ij}^{FC}(f_i, f_j) = \sum_{i \in S} \sum_{j \in N_i} (f_i - f_j)^2 \times (1 - ED(i, j)) \quad (21)$$

3.3. Space constraint

Because of the similarity in intensities between the tumor and other hypoechoic regions, the intensity based algorithms cannot segment the tumors accurately. In this section, three categories of space information – tumor pose, position and intensity distribution – are utilized to exclude the normal regions in the ROI. The tumor pose and position are important features for distinguishing benign and malignant tumors [26]; and they are calculated on the initial ROI (ROI_0) and invariant to the brightness and contrast. The space term E^{SC} is defined as

$$E^{SC}(f|y_{ROI}) = \sum_{i \in S} -\ln(V_i^{PP} \cdot V_i^A(f_i|y_{ROI})) + \sum_{i \in S} \sum_{j \in N_i} V_{ij}^A(f_i, f_j|y_{ROI}) \quad (22)$$

where V_i^{PP} is the constraint based on tumor position and pose, V_i^A and V_{ij}^A are the constraints based on the intensity distribution.

3.3.1. Position and pose constraints

We constrain the position and pose of the tumor by using the 2D elliptical Gaussian function:

$$V_i^{PP}(f_i|y_{ROI}) = (1 - f_i) + (2f_i - 1)G(i) \quad (23)$$

$$G(i) = \exp\{-[a(i_x - x_0)^2 + 2b(i_x - x_0)(i_y - y_0) + c(i_y - y_0)^2]\} \quad (24)$$

where f_i is the label (0 or 1) of the i th pixel, (x_0, y_0) and (i_x, i_y) represent the coordinates of the center and the i th pixel, respectively; and a, b and c are used to control the spread and pose of the Gaussian blob. The parameters a, b and c are given by

$$a = \frac{\cos^2 \theta}{2\sigma_x^2} + \frac{\sin^2 \theta}{2\sigma_y^2}, b = -\frac{\sin 2\theta}{4\sigma_x^2} + \frac{\sin 2\theta}{4\sigma_y^2}, c = \frac{\sin^2 \theta}{2\sigma_x^2} + \frac{\cos^2 \theta}{2\sigma_y^2} \quad (25)$$

respectively, where θ is the orientation of the major axis of the Gaussian blob relative to the horizontal direction, and σ_x and σ_y are the standard deviations along the major axis and minor axis, respectively. We define σ_x and σ_y as the half of the length of major axis (l) and the minor axis (m), respectively. Although we use the elliptical Gaussian function to model the position and pose of the tumor, it could be applied to the tumors with any shape validated by experiments.

3.3.2. Constraints by image intensity

Some segmentation methods modeled the intensity distribution of the BUS image using Rayleigh, Gaussian, exponential and Gamma distribution, but the predefined distributions may not match the real situation well when the BUS images are captured from different devices or taken under different device settings. In this section, we will define the intensity distribution by using the foreground and background histograms of the image without assumption of intensity distribution, which will be more robust than traditional methods. The first order constraint is defined as

$$V_i^A(f_i|y_{ROI}) = \Pr(x=y_i | l=f_i) \quad (26)$$

where $\Pr(x=y_i | l=f_i)$ is the class-conditional probability density function for x given the label $l \in \{0, 1\}$, y_i is the intensity of pixel i , and f_i is the label assigned to i . $\Pr(x|\mathbf{0})$ and $\Pr(x|\mathbf{1})$ are defined as the two histograms $h_1(ROI_0)$ and $h_2(\overline{ROI_0})$ (refer Eqs. (14) and (15)), respectively. The second order term V_{ij}^A is defined as the penalty on the discontinuities between two neighboring pixels, and is given by

$$V_{ij}^A(f_i, f_j|y_{ROI}) = (f_i - f_j)^2 \cdot \exp\{-(y_i - y_j)^2 / 2\sigma^2\} / D_e(i, j) \quad (27)$$

where D_e measures the Euclidean distance between the corresponding neighboring pixels; and y_i and y_j are the intensities of pixels i and j , respectively. Eq. (27) penalizes the pixels with the same label more when $|y_i - y_j| < \delta$; and δ is 20 (pixels) determined by experiments.

The task is to segment the tumor from BUS image and the label set is $L=\{\mathbf{0}, \mathbf{1}\}$. The cost function is graph-representable, since $(V_{ij}^{FC}(0,0)+V_{ij}^{FC}(1,1)+V_{ij}^A(0,0)+V_{ij}^A(1,1)\leq V_{ij}^{FC}(0,1)+V_{ij}^{FC}(1,0)+V_{ij}^A(0,1)+V_{ij}^A(1,0))$, and can be optimized by max-flow min-cut algorithm globally [37].

4. Experimental results

4.1. Dataset

The performance of the proposed method was evaluated by using a B-mode BUS image dataset of 184 cases (93 benign and 91 malignant). The images are collected by the Second Affiliated Hospital of Harbin Medical University using two kinds of medical imaging systems: VIVID 7 (GE) and EUB-6500 (Hitachi). In this study, informed consents to the protocol from all patients were acquired.

An experienced radiologist's manually delineated tumor boundaries were used as the golden standards [13,15–17]. The

proposed automatic segmentation algorithm was implemented by using Matlab (R2012a, MathWorks Inc., MA). All experiments were performed on a windows-based PC equipped with a dual-core (3.3 GHz) processor and 4 GB memory. The performance of the proposed fully automatic breast tumor segmentation algorithm was validated by comparing the results with the golden standards.

Table 1
Performances of seed generation algorithms.

Metrics	The method in [17]			The proposed method			
	Classes	Correct	Accuracy (%)	Time (s)	Correct	Accuracy (%)	Time (s)
Benign (93)		89	94.68	0.589	93	100	0.065
Malignant (91)		88	96.70	0.530	91	100	0.054
Total (184)		177	95.68	0.547	184	100	0.060

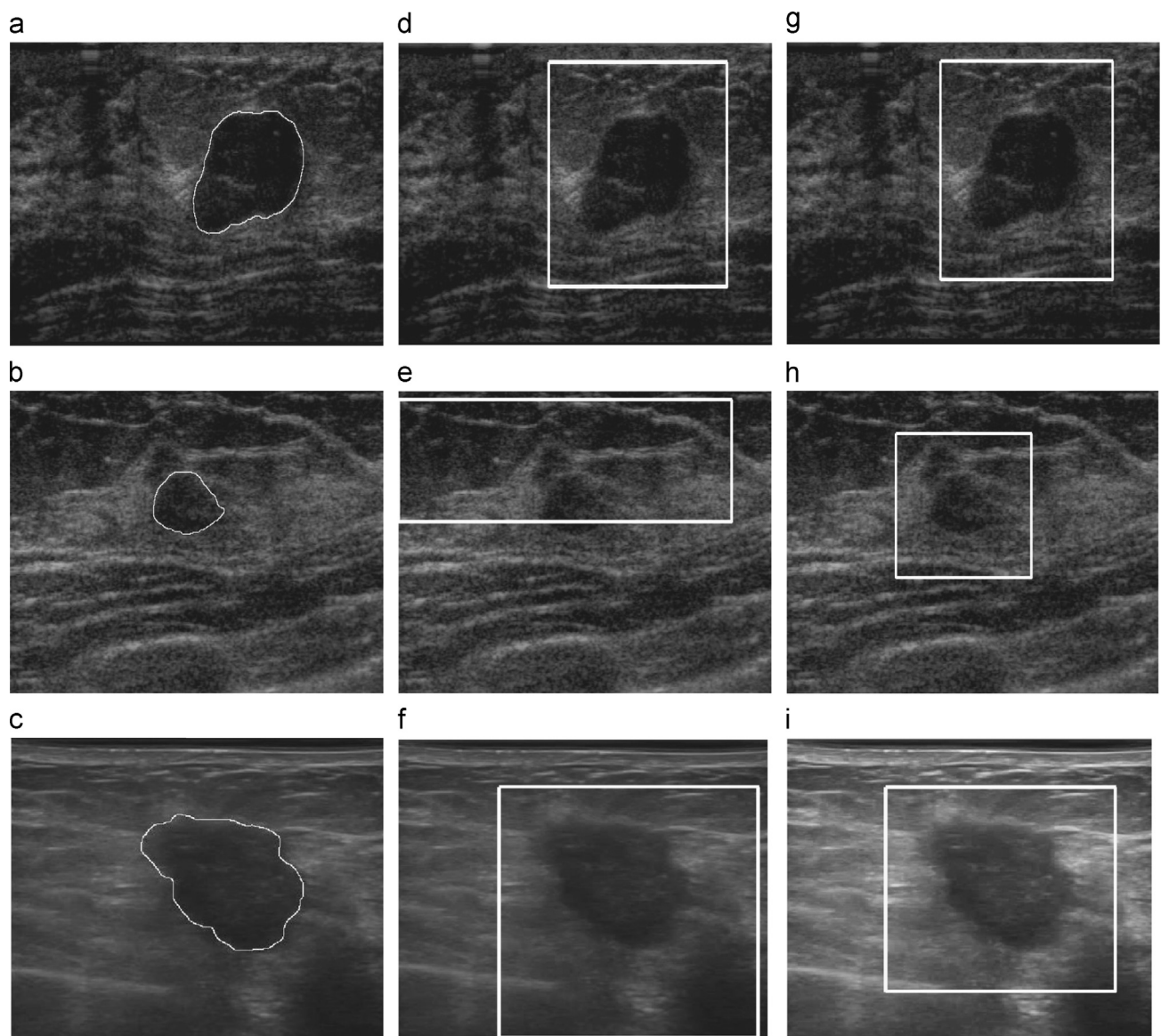


Fig. 5. ROI generation of three BUS images: (a)–(c) the original images with delineation of an experienced radiologist; (d)–(f) the ROIs (white rectangles) generated by the method in [17]; and (g)–(i) the ROIs (white rectangles) generated by the proposed method.

4.2. Metrics and parameters

In the proposed ROI generation algorithm, three intermediate results (*seed*, ROI_0 and ROI_t) were generated. In Section 4.3.1, the precision of the seed generation algorithm was validated by calculating the percentage of the correct seeds on the images in the dataset. In Section 4.3.2, average precision rate (APR) and average recall rate (ARR) were calculated to evaluate the performance of the ROI generation algorithm. APR and ARR were calculated by using the following equations.

$$APR_{ROI} = \frac{1}{N_T} \sum_{i=1}^{N_T} (N_i^{DR}/N_i^D), \quad ARR_{ROI} = \frac{1}{N_T} \sum_{i=1}^{N_T} (N_i^{DR}/N_i^R)$$

In the above equations, N_T is the number of images; N_i^{DR} the overlapped area (number of pixels) between ROI_t and the true tumor area, N_i^D is the size (number of pixels) of ROI_t , and N_i^R is size of the tumor region of image i .

The commonly used area and boundary error metrics were employed to assess the performance of the proposed segmentation approach. The area error metrics include the true positive ratio (TPR), false positive ratio (FPR) and similarity ratio (SIR).

$$TPR = |A_m \cap A_r|/|A_m|, \quad FPR = |A_m \cup A_r - A_m|/|A_m|,$$

$$SIR = |A_m \cap A_r|/|A_m \cup A_r|$$

Table 2
Performances of ROI generation algorithms.

Metrics	The method in [17]			The proposed method		
	APR (%)	ARR (%)	Time (s)	APR (%)	ARR (%)	Time (s)
Classes						
Benign (93)	96.26	25.83	0.608	99.13	27.69	0.232
Malignant (91)	96.92	26.98	0.547	99.33	30.91	0.192
Total (184)	96.58	26.39	0.574	99.39	29.29	0.213

where A_m is the pixel set of the tumor region outlined by the radiologist manually, and A_r is the pixel set of the tumor region generated by the proposed method. Furthermore, average Hausdorff error (AHE) and average mean absolute error (AME) [15] were used to measure the worst possible disagreement and the average agreement between two boundaries, respectively.

The log-Gabor responses are calculated along four orientations (N_{ori}) and at four scales (N_{sca}), $\omega_0 = 1/3 \times 2.1^{ns}$, $\kappa = 0.55$ and $\sigma_\phi = \pi/(1.2 \times N_{ori})$. By experiments, the log-Gabor filters with four directions and four scales are good enough for achieving

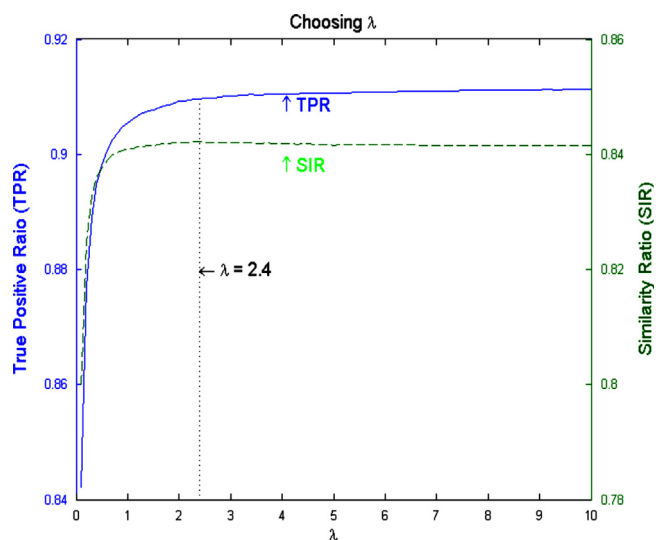


Fig. 7. TPR (solid) and SIR (dashed) of the proposed segmentation method as the functions of λ . The intersection between the vertical dotted line ($\lambda=2.4$) and the SIR indicates the maximum of the SIR value.

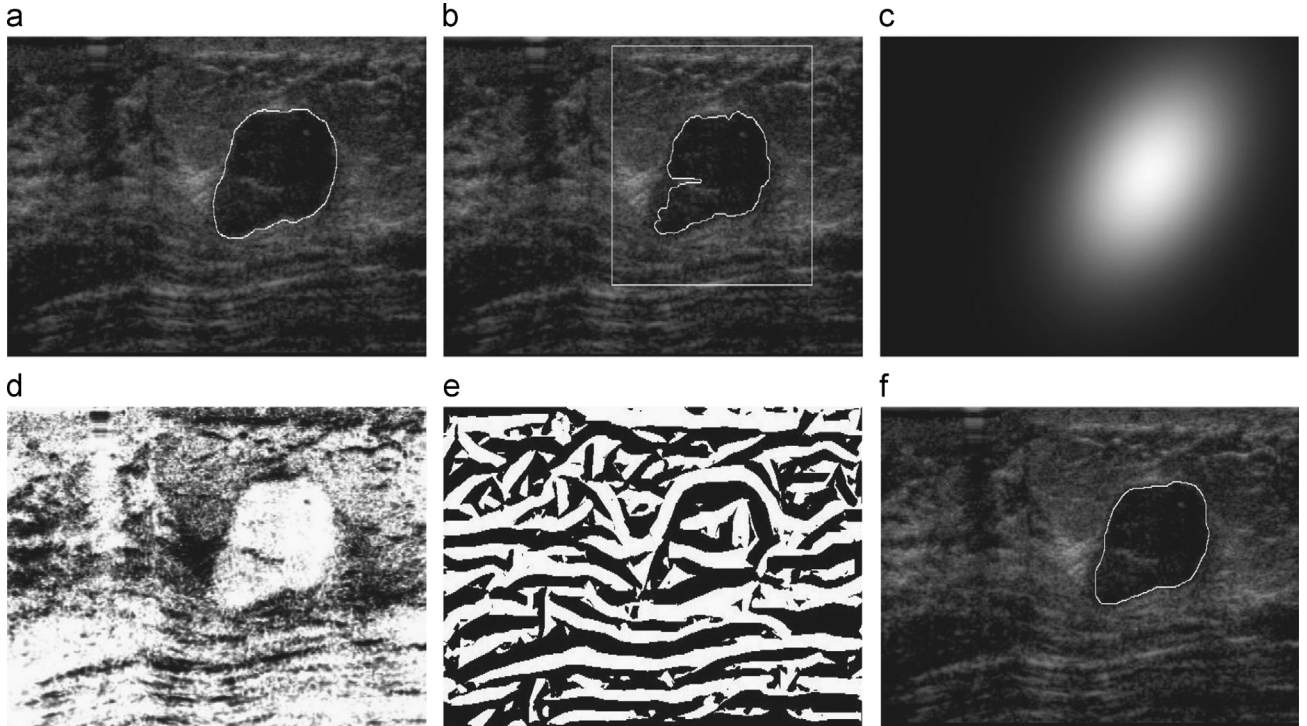


Fig. 6. The intermediate results of the proposed method: (a) the original image with boundary delineated by the radiologist; (b) the ROI generated by the proposed method; (c) the output of the pose and position model; (d) the output of the h_1 ; (e) the output of the proposed edge detector; and (f) the tumor region segmented by the proposed method.

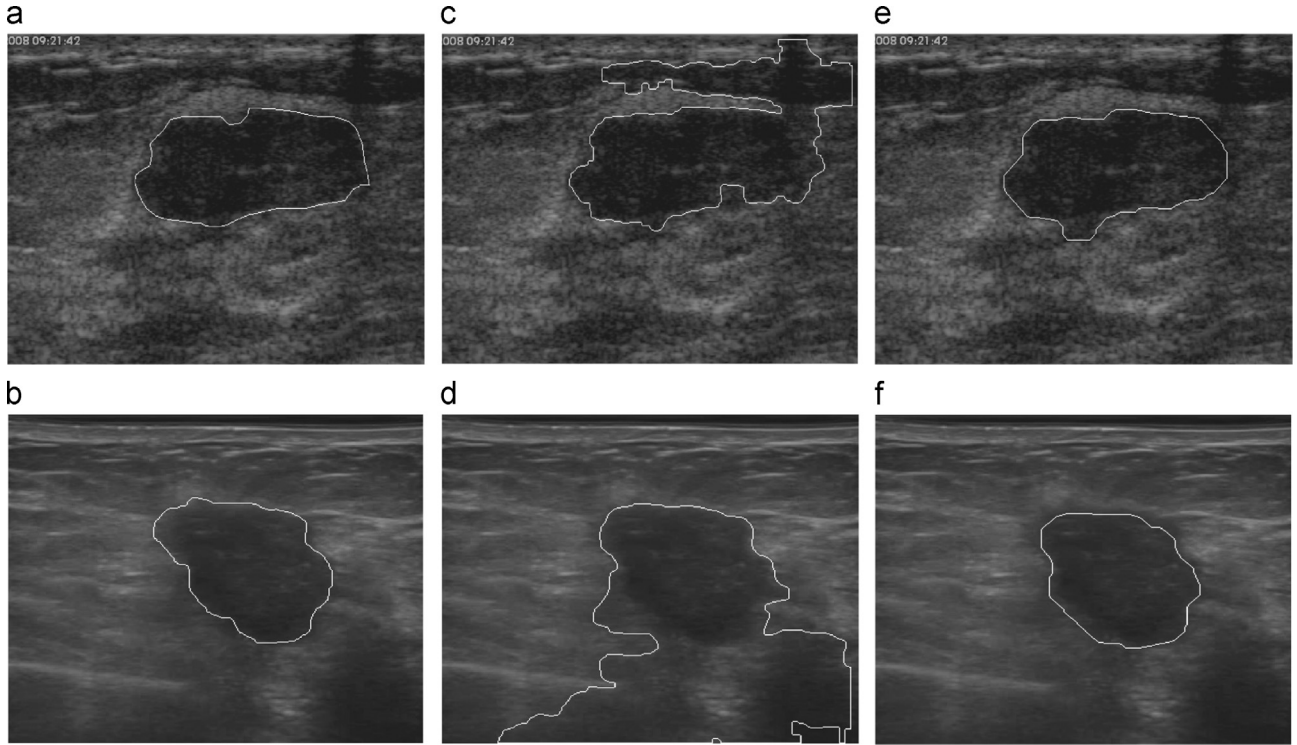


Fig. 8. The segmentation of BUS images with fat region close to the tumor or with low contrast: (a)–(b) the original images with tumor regions manually delineated by the radiologist; (c)–(d) The tumor regions generated by the method proposed in [17]; (e)–(f) the tumor regions produced by the proposed method.

acceptable results; otherwise, more computational time is needed. The σ in V_{ij}^A is selected as 20 (pixels) in the experiments.

4.3. ROI generation

4.3.1. Seed generation

The proposed method and the methods in [15] and [17] are employed for comparison, and the seed generation results (white points on images) are shown in Fig. 4. Comparing with the tumor boundaries delineated by the experienced radiologist (Fig. 4(a–c)), it demonstrated that all of the seeds generated by the proposed method are in the tumor regions (Fig. 4(j–l)); Fig. 4(d and g) show that the seed generation algorithm in [15] and [17] can also locate the seeds correctly when the tumors are close to their fixed RPs (image centers); however, as shown in Fig. 4(e, f and i), when the tumors are far away from the fixed RPs, the method in [15] produces wrong seeds; and when the tumor is close to the upper fat region, the method in [17] will fail to generate the seed correctly.

Both of the two seed generation methods in [15] and [17] used the image centers as the predefined RPs. In [15], the distance from a point to the RP is a key factor to determine whether the point is the seed or not. When the actual tumors are not close to the predefined RP, the method cannot generate the right seeds. The overall accuracy of the seed generation method in [15] is only 76.76% using the same dataset, which is quite low and we will not compare this method in further experiments. The overall performances of proposed seed generation method and method in [17] based on the same database are listed in Table 1. The proposed seed generation method achieves 100% accuracy. Even the method in [17] achieves lower accuracy (95.68%) comparing with that of the proposed approach; its processing speed is almost ten times slower than the proposed method as shown in Table 1.

Table 3
Statistical evaluation with area and boundary error metrics.

Metrics	Area error metrics			Boundary error metrics	
	Methods	TPR (%)	FPR (%)	SIR (%)	AHE (%)
Method in [17]		92.58	37.58	78.17	24.35
The proposed method		91.23	9.97	83.73	20.43

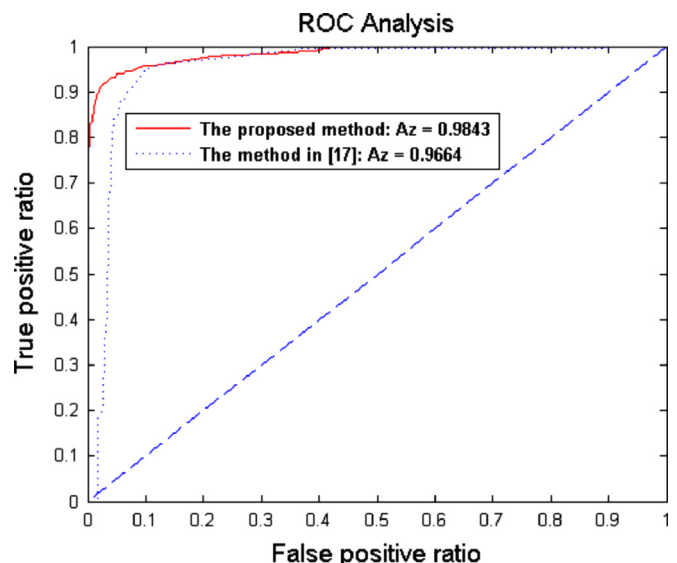


Fig. 9. ROC curves of the two methods.

4.3.2. ROI generation

The ROI generation results of three BUS images are shown in Fig. 5. The tumor boundaries were delineated by an experienced radiologist (Fig. 5(a–c)). As shown in Fig. 5(d–f), and (g–i), both the method in [17] and the proposed method can locate the ROI of Fig. 5(a) with high accuracy; however, the proposed ROI generation method is more robust and accurate even when there exists a fat region close to the tumor area (Fig. 5(b)) or the image contrast is low (Fig. 5(c)).

The overall performances of the proposed ROI generation method and the method in [17] are shown in Table 2. The APR of the proposed method on the total cases is 99.39%, which is higher than that of the method in [17]. The higher ARRs indicate that the ROIs generated by the proposed method can exclude more normal regions.

4.4. Tumor segmentation

The intermediate results of the proposed segmentation method are shown in Fig. 6.

4.4.1. Choosing tuning parameter λ

The tuning parameter λ controls the relative impact of the space constraint and the frequency constraint on the segmentation. When $\lambda=0$, the space term has no effect, and the segmentation method degrades into the frequency domain edge detector (ED). As λ increases, the impact of the space term grows, leading to a segmentation method constructed on two domains.

When λ is extremely large, the edge detector ED will lose its effect. Fig. 7 displays the FPR and SIR of the proposed segmentation method applied to the BUS dataset. The solid curve and the dashed curve show the TPR and the SIR as the functions of λ , respectively. As λ increases from 0 to 1.5, the increased impact of space term leads to a substantial increasing in FPR and SIR. Beyond this point, the increases in TPR and SIR slow down. When λ reaches 2.4, the SIR arrives at its maximum. Because the SIR is more comprehensive than the other metrics, it will be used to determine the value of λ .

4.4.2. Segmentation results

Employing the same database, we compared the proposed method with the currently published method in [17]. The segmentation results of two BUS images are shown in Fig. 8. In Fig. 8(a), the tumor is close to the subcutaneous fat region, the method in [17] fails to exclude the fat region from the tumor region (Fig. 8(c)). Fig. 8(b) shows a low-contrast BUS image which is captured by another imaging device. As shown in Fig. 8(d and f), the proposed method can segment the tumors accurately even the contrast is low, while the method in [17] cannot exclude the shadow regions.

The overall performance of the proposed method is shown in Table 3. The high average TPR (92.58%) of the methods in [17] demonstrates that the tumor regions generated by the method overlapped the true tumor regions with high percentage. However, its high average FPR (37.58%) and relatively low SIR indicate that the method cannot distinguish the normal tissues from the tumor region well. The results of the boundary error metrics also show that the proposed method achieved much better overall performance than that of the method in [17]. The receiver operating characteristic (ROC) curves of the proposed method and the method in [17] are shown in Fig. 9.

5. Conclusion

In this paper, a novel fully automatic BUS image segmentation method is proposed. This approach can model both the space and

frequency domain knowledge to perform the tumor segmentation under a probability framework. The experiments demonstrate that both of the proposed ROI generation method and tumor segmentation method are more accurate and robust than the existing methods.

The excellent results are due to the following reasons: (1) the proposed methods are based on solid biologic foundations from breast anatomy; (2) the proposed segmentation framework incorporates constraint from the frequency domain with the prior knowledge from the space domain, which makes the results more accurate; (3) the newly proposed edge detector in the frequency domain is invariant to the image brightness and contrast, which makes the proposed method more robust than the traditional gradient-based methods; and (4) the proposed cost function is graph-representable and its global optimum can be found quickly by using the max-flow min-cut algorithm.

Conflict of interest

None declared.

Acknowledgements

This work is supported, in part, by the National Science Foundation of China; the grant numbers is 61100097.

References

- [1] H.D. Cheng, J. Shan, W. Ju, Y.H. Guo, L. Zhang, Automated breast cancer detection and classification using ultrasound images: a survey, *Pattern Recognit.* 43 (2010) 299–317.
- [2] R. Siegel, D. Naishadham, A. Jemal, *Cancer statistics, 2012*, CA-Cancer J. Clin. 62 (2012) 10–29.
- [3] H.D. Cheng, X.J. Shi, R. Min, L.M. Hu, X.R. Cai, H.N. Du, Approaches for automated detection and classification of masses in mammograms, *Pattern Recognit.* 39 (2006) 646–668.
- [4] B.O. Anderson, R. Shyyan, A. Eniu, R.A. Smith, C.H. Yip, N.S. Bese, L.W. Chow, S. Masood, S.D. Ramsey, R.W. Carlson, Breast cancer in limited-resource countries: an overview of the breast health global initiative 2005 guidelines, *Breast J.* 12 (2006) S3–S15.
- [5] K. Drukker, M.L. Giger, C.J. Vyborny, E.B. Mendelson, Computerized detection and classification of cancer on breast ultrasound, *Acad. Radiol.* 11 (2004) 526–535.
- [6] C.M. Sehgal, S.P. Weinstein, P.H. Arger, E.F. Conant, A review of breast ultrasound, *J. Mammary Gland Biol. Neoplasia* 11 (2006) 113–123.
- [7] D.R. Chen, R.F. Chang, Y.L. Huang, Breast cancer diagnosis using self-organizing map for sonography, *Ultrasound Med. Biol.* 26 (2000) 405–411.
- [8] Y.L. Huang, D.R. Chen, Y.K. Liu, Breast cancer diagnosis using image retrieval for different ultrasonic systems, in: Proceedings of IEEE ICIP, 2004, pp. 2957–2960.
- [9] K. Horsch, M.L. Giger, C.J. Vyborny, L.A. Venta, Performance of computer-aided diagnosis in the interpretation of lesions on breast sonography, *Acad. Radiol.* 11 (2004) 272–280.
- [10] B. Liu, H.D. Cheng, J.H. Huang, J.W. Tian, X.L. Tang, J.F. Liu, Fully automatic and segmentation-robust classification of breast tumors based on local texture analysis of ultrasound images, *Pattern Recognit.* 43 (2010) 280–298.
- [11] J.G. Bosch, S.C. Mitchell, B.P. Lelieveldt, F. Nijland, O. Kamp, M. Sonka, J. H. Reiber, Automatic segmentation of echocardiographic sequences by active appearance motion models, *IEEE Trans. Med. Imaging* 21 (2002) 1374–1383.
- [12] J. Shan, H.D. Cheng, Y.X. Wang, A novel automatic seed point selection algorithm for breast ultrasound images, in: Proceedings of ICPR, 2008, pp. 3990–3993.
- [13] J. Shan, Y. Wang, H.-D. Cheng, Completely automatic segmentation for breast ultrasound using multiple-domain features, in: Proceedings of IEEE ICIP, 2010, pp. 1713–1716.
- [14] K. Drukker, M.L. Giger, K. Horsch, M.A. Kupinski, C.J. Vyborny, E.B. Mendelson, Computerized lesion detection on breast ultrasound, *Med. Phys.* 29 (2002) 1438–1446.
- [15] A. Madabhushi, D.N. Metaxas, Combining low-, high-level and empirical domain knowledge for automated segmentation of ultrasonic breast lesions, *IEEE Trans. Med. Imaging* 22 (2003) 155–169.
- [16] B. Liu, H.D. Cheng, J.H. Huang, J.W. Tian, J.F. Liu, X.L. Tang, Automated segmentation of ultrasonic breast lesions using statistical texture classification and active contour based on probability distance, *Ultrasound Med. Biol.* 35 (2009) 1309–1324.

- [17] J. Shan, H.D. Cheng, Y.X. Wang, Completely automated segmentation approach for breast ultrasound images using multiple-domain features, *Ultrasound Med. Biol.* 38 (2012) 262–275.
- [18] X. Liu, Z. Huo, J. Zhang, Automated segmentation of breast lesions in ultrasound images, in: Proceedings of IEEE Engineering in Medicine and Biology Society, EMBS 2005, 2006, pp. 7433–7435.
- [19] C.K. Yeh, S.J. Miao, W.C. Fan, Y.S. Chen, Automatic ultrasonic breast lesions detection using support vector machine based algorithm, in: Proceedings of SPIE, vol. 6513, 2007, pp. 651317(1–8).
- [20] S. Lee, Q. Huang, L. Jin, M. Lu, T. Wang, A. Graph-Based, Segmentation method for breast tumors in ultrasound images, in: Proceedings of IEEE iCBBE, 2010, pp. 1–4.
- [21] Y.L. Huang, D.R. Chen, Watershed segmentation for breast tumor in 2-D sonography, *Ultrasound Med. Biol.* 30 (2004) 625–632.
- [22] M. Yap, E.A. Edirisonghe, H.E. Bez, Fully automatic lesion boundary detection in ultrasound breast images, *Proc. SPIE* 6512 (2007) 651231 (1–8).
- [23] M. Xian, J. Huang, Y. Zhang, X. Tang, Multiple-domain knowledge based MRF model for tumor segmentation in breast ultrasound images, in: Proceedings of IEEE ICIP, 2012, pp. 2021–2024.
- [24] C.G. Rafael, E.W. Richard, Image smoothing using frequency domain filters, in: Digital Image Processing, third ed. Prentice-Hall, Inc., 2006, pp. 298–299.
- [25] D.P. Doane, L.E. Seward, Measuring skewness: a forgotten statistic? *J. Stat. Educ.* 19 (2011) 1–18.
- [26] A.T. Stavros, Breast anatomy: the basis for Understanding Sonography, in: Breast ultrasound. LWW, Philadelphia, 2004, pp. 56–59.
- [27] Y.Z. Cheng, Mean Shift, Mode seeking, and clustering, *IEEE Trans. Pattern Anal. Mach. Intell.* 17 (1995) 790–799.
- [28] D. Comaniciu, P. Meer, Mean shift: a robust approach toward feature space analysis, *IEEE Trans. Pattern Anal. Mach. Intell.* 24 (2002) 603–619.
- [29] L. Vincent, Morphological grayscale reconstruction in image analysis: applications and efficient algorithms, *IEEE Trans. Image Process* 2 (1993) 176–201.
- [30] N. Otsu, A threshold selection method from gray-level histograms, *Automatica* 11 (1975) 23–27.
- [31] D.R. Chittajallu, G. Brunner, U. Kurkure, R.P. Yalamanchili, I.A. Kakadiaris, Fuzzy-cuts: a knowledge-driven graph-based method for medical image segmentation, in: Proceedings of IEEE CVPR, 2009, pp. 715–722.
- [32] J.A. Noble, Ultrasound image segmentation and tissue characterization, *Proc. Inst. Mech. Eng. Part H – J. Eng. Med.* 224 (2010) 307–316.
- [33] M.C. Morrone, J. Ross, D.C. Burr, R. Owens, Mach bands are phase dependent, *Nature* 324 (1986) 250–253.
- [34] M.C. Morrone, R. Owens, Feature detection from local energy, *Pattern Recognit. Lett.* 6 (1987) 303–313.
- [35] P. Kovesi, Image features from phase congruency, *Videre: J. Comput. Vis. Res.* 1 (1999) 1–26.
- [36] S. Mallat, Zero-crossings of a wavelet transform, *IEEE Trans. Inf. Theory* 37 (1991) 1019–1033.
- [37] V. Kolmogorov, R. Zabin, What energy functions can be minimized via graph cuts? *IEEE Trans. Pattern Anal. Mach. Intell.* 26 (2004) 147–159.
- [38] A. Briassouli, N. Ahuja, Fusion of frequency and spatial domain information for motion analysis, in: Proceedings of ICPR, 2004, pp. 175–178.
- [39] A. Briassouli, N. Ahuja, Integrated spatial and frequency domain 2D motion segmentation and estimation, in: Proceedings of ICCV, 2005, pp. 244–250.
- [40] Z. Kato, T.C. Pong, A Markov random field image segmentation model for color textured images, *Image Vis. Comput.* 24 (2006) 1103–1114.

Min Xian received B.S. degree in Information Security from Harbin Institute of Technology, Harbin, China, in 2008, and the M.S. degree in Pattern Recognition and Intelligence System from Harbin Institute of Technology, Harbin, China, in 2011. He is now a Ph.D. student in the Department of Computer Science, Utah State University. His current research interests include medical image processing, pattern recognition, machine learning, and neutrosophic logic.

Heng-Da Cheng received Ph.D. degree in Electrical Engineering from Purdue University (Supervisor: Prof. K.S. Fu), West Lafayette, IN, 1985. Now, he is a Full Professor, Department of Computer Science, and an Adjunct Full Professor, Department of Electrical Engineering, Utah State University, Logan, Utah. Dr. Cheng is an Adjunct Professor and Doctoral Supervisor of Harbin Institute of Technology. He is also a Guest Professor of the Institute of Remote Sensing Application, Chinese Academy of Sciences, a Guest Professor of Wuhan University, a Guest Professor of Shantou University, and a Visiting Professor of Northern Jiaotong University.

Dr. Cheng has published more than 300 technical papers and is the Co-editor of the book, *Pattern Recognition: Algorithms, Architectures and Applications* (World Scientific Publishing Co., 1991). His research interests include image processing, pattern recognition, computer vision, artificial intelligence, medical information processing, fuzzy logic, genetic algorithms, neural networks, parallel processing, parallel algorithms, and VLSI architectures.

Dr. Cheng is the General Chair of the 11th Joint Conference on Information Sciences (JCIS 2008), was the General Chair of the 10th Joint Conference on Information Sciences (JCIS 2007), was the General Chair of the Ninth Joint Conference on Information Sciences (JCIS 2006), was the General Chair of the Eighth Joint Conference on Information Sciences (JCIS 2005), General Chair and Program Chair of the Sixth International Conference on Computer Vision, Pattern Recognition and Image Processing (CVPRIP 2007), General Chair and Program Chair of the Sixth International Conference on Computer Vision, Pattern Recognition and Image Processing (CVPRIP 2006), General Chair and Program Chair of the Sixth International Conference on Computer Vision, Pattern Recognition and Image Processing (CVPRIP 2005), and was the General Chair and Program Chair of the Fifth International Conference on Computer Vision, Pattern Recognition and Image Processing (CVPRIP 2003), and was the General Chair and Program Chair of the Fourth International Conference on Computer Vision, Pattern Recognition and Image Processing (CVPRIP 2002), the General Chair and Program Chair of the Third International Conference on Computer Vision, Pattern Recognition and Image Processing (CVPRIP 2000), the General Chair and Program Chair of the First International Workshop on Computer Vision, Pattern Recognition and Image Processing (CVPRIP 1998), and the Program Co-Chairman of Vision Interface 1990. He served as program committee member and Session Chair for many conferences, and as reviewer for many scientific journals and conferences. Dr. Cheng has been listed in Who's Who in the World, Who's Who in America, Who's Who in Communications and Media, Who's Who in Finance and Industry, Who's who in Science and Engineering, Men of Achievement, 2000 Notable American Men, International Leaders in Achievement, 500 Leaders of Influence, International Dictionary of Distinguished Leadership, etc.

Dr. Cheng is also an Associate Editor of *Pattern Recognition*, an Associate Editor of *Information Sciences* and Associate Editor of *New Mathematics and Natural Computation*.

Yingtao Zhang received her M.S. degree from Computer Science School of Harbin Institute of Technology, Harbin, China, in 2004, and the Ph.D. degree in Pattern Recognition and Intelligence System from Harbin Institute of Technology, Harbin, China, in 2010. Now, she is an associate professor, School of Computer Science and Technology, Harbin Institute of Technology, Harbin, China. Her research interests include pattern recognition, computer vision and medical image processing.